

Geometry and Scaling Laws of Excursion and Iso-sets of Enstrophy and Dissipation in Isotropic Turbulence

José Hugo Elsas^{1,2}, Alexander S. Szalay³ and Charles Meneveau¹

¹*Department of Mechanical Engineering, Johns Hopkins University;* ²*Instituto de Física, Universidade Federal do Rio de Janeiro;* ³*Department of Physics and Astronomy and Department of Computer Science, Johns Hopkins University*

Motivated by interest in the geometry of high intensity events of turbulent flows, we examine spatial correlation functions of sets where turbulent events are particularly intense. These sets are defined using indicator functions on excursion and iso-value sets. Their geometric scaling properties are analyzed by examining possible power-law decay of their radial correlation function. We apply the analysis to enstrophy, dissipation, and velocity gradient invariants Q and R and their joint spatial distributions, using data from a direct numerical simulation of isotropic turbulence at $Re_\lambda \approx 430$. While no fractal scaling is found in the inertial range using box-counting in the finite Reynolds number flow considered here, power-law scaling in the inertial range is found in the radial correlation functions. Thus a geometric characterization in terms of these sets' correlation dimension is possible. Strong dependence on the enstrophy and dissipation threshold is found, consistent with multifractal behavior. Nevertheless the lack of scaling of the box-counting analysis precludes direct quantitative comparisons with earlier work based on the multifractal formalism. Surprising trends, such as a lower correlation dimension for strong dissipation events compared to strong enstrophy events, are observed and interpreted in terms of spatial coherence of vortices in the flow. We show that sets defined by joint conditions on strain and enstrophy, and on Q and R , also display power law scaling of correlation functions, providing further characterization of the complex spatial structure of these intersection sets.

I. INTRODUCTION

Dissipation rate and enstrophy have been observables of great interest in turbulence research due to their dynamical significance for the evolution of the flow and their rich spatial structure and intermittent nature [1]. In a view dating back to Kolmogorov [2, 3] and Obukhov [4] the transfer of kinetic energy from large to small scales proceeds as a self similar cascade process accompanied with increasing intermittency of intense events, and these are often associated with large values of dissipation rate and enstrophy. The presence of power-laws in the velocity spectrum, velocity structure functions and moments of velocity gradients and dissipation are seen as indication of such self-similar behavior.

One of the most common ways to study the resultant intermittent behavior has been through the multifractal formalism. It has its origin in works by Kolmogorov [3] and Obukhov [4] who assumed a lognormal distribution for the dissipation rate, with alternative models proposed by Novikov & Stewart [5], Novikov [6–8], Mandelbrot [9] and Frisch et al [10]. The multifractal approach was formalized explicitly in Benzi et al. [11], making connections to fractal geometry.

In such methodology, special attention is paid to the power-law scaling of high-order moments of velocity increments (structure functions) or dissipation rates. The approach then invokes a continuous distribution of fractal dimensions $D(h)$ of spatial sets where the velocity increments across a distance r scale with a local Holder exponent h , according to $|u(x+r) - u(x)| \sim r^h$ [11] ($u(x)$ is a component of the fluid velocity and r is a displacement in the same direction). A description in terms of local scaling for the dissipation rate ϵ and the distribution of its local exponents α with a fractal dimension $f(\alpha)$ has also been used [12, 13]. The multifractal formalism as applied to turbulence has been reviewed in Refs. [1, 14, 15]. In this formalism the directly measured quantities are the various statistical moments such as $\langle |u(x+r) - u(x)|^p \rangle$ or $\langle \epsilon_r^q \rangle$ (where ϵ_r is the dissipation averaged in a box of size r) while the fractal dimension functions $D(h)$ and $f(\alpha)$ are determined indirectly using the Legendre transformation [1] applied to the scaling exponents of the moments. The majority of these prior data analyses were done using one-dimensional experimental surrogates for dissipation rates while only in the last decade have full three-dimensional Direct Numerical Simulations (DNS) begun to approach high enough Reynolds numbers for the possible power law scaling to be discernible [16, 17].

In spite of the significant success of the multifractal formalism to encapsulate many different phenomena observed since (e.g. multi-point correlations [18], time correlations [19], extended self-similarity [20] and varying viscous scales [21]), direct determination of the fractal dimensions as a geometric characterization of the sets of high intensity events has been far less common. An early attempt to study the scale-invariance of histograms of singularities [22] and to deduce the dimension from these scalings have met with mixed

success due to strong finite-size corrections and was thus limited to data at very high Reynolds numbers.

Thus, the status of power-law scaling of geometric features of strong events in turbulence remains unsettled. In the present work we seek a geometric characterization of high-intensity events in turbulence that does not rely on statistical moments of the variable but that identifies the high intensity regions directly based on thresholding of the respective variables of interest. Specifically, we ask whether power-law scaling can be identified for such geometric sets, at Reynolds numbers attainable with direct numerical simulations (DNS). In seeking such direct geometric observables and their possible power-law scaling we are also motivated by other fields. For instance, the scaling analysis of geometrical properties of excursion sets has been applied for random sets in probability theory and the theory of random fields [23], and also have been used for analysis of matter distributions in cosmology [24–26].

In this study we employ a direct way to study regions of varying intensity of enstrophy and dissipation rate: Instead of computing moments of the observable (or box-averaged observable) itself, we first define a geometric set as the set of points where the variables exceed a threshold (or fall into a range of values). We use the indicator function that takes on a value of 1 inside the set of interest and zero outside. Such geometric sets form convoluted clusters of complicated shapes. For example, high-intensity regions of vorticity are known to be arranged into elongated (worm-like) structures, representing vortices [27, 28]. Nominally each one of these structures would be characterized by a dimension equal to unity. However, it is also well known that these vortices are clustered into regions with possible multi-scaling properties and the scaling of a collection of such vortices is not necessarily obvious. Conversely, high dissipation events are often thought to be distributed along sheets, although again these may have complex spatial structure not necessarily leading to a dimension of two. Once the set is identified, we then compute its two-point correlation function and seek to identify possible inertial-range power-law decay of the tails of the correlation functions. We also perform a direct box-counting analysis of these sets to establish whether direct fractal scaling can be identified in the inertial range of turbulence.

Furthermore, we extend the analysis to the geometry of sets where both dissipation and enstrophy take on certain values. A “joint multifractal” formalism was introduced previously [29], but was also based on scaling of joint moments rather than directly based on possible fractal scaling of the geometric objects that arise from joint distributions of enstrophy and dissipation. Besides enstrophy and dissipation, we also explore the spatial structure of sets formed by two velocity gradient invariants Q and R , observables that have elicited considerable interest in recent years [30]. The dataset to be considered for this analysis is isotropic turbulence at a Taylor-scale Reynolds number of $Re_\lambda \approx 433$ obtained from DNS of forced Navier-Stokes equations [31]. We first define the variables of interest and then apply the analysis to the various quantities and joint distributions.

II. DEFINITIONS AND DATA SET

The typical observables we are interested in are scalar quantities derived from the velocity gradient tensor $\nabla \mathbf{u}$. These scalar fields describe the rate of rotation (based on the antisymmetric part of $\nabla \mathbf{u}$) and the rate of fluid material deformation (via the symmetric part of $\nabla \mathbf{u}$). Specifically, the two scalar fields that will be considered are defined according to

$$\frac{1}{2}\omega^2(\mathbf{x}) = \frac{1}{2}(\nabla \times \mathbf{u})^2 = \frac{1}{2}\epsilon_{ijk}\epsilon_{klm}\partial_i u_j \partial_l u_m \quad (1)$$

$$S^2(\mathbf{x}) = S_{ij}S_{ij}, \quad \text{where} \quad (2)$$

$$S_{ij} = \frac{1}{2}(\nabla \mathbf{u} + \nabla \mathbf{u}^T)_{ij} = \frac{1}{2}(\partial_i u_j + \partial_j u_i) \quad (3)$$

Note that the dissipation is given by $\epsilon(\mathbf{x}) = 2\nu S^2(\mathbf{x})$, where ν is the fluid kinematic viscosity. Hence we refer to S^2 as the dissipation henceforth. A significant number of prior studies have focused on dissipation and enstrophy such as [32–35], also, other observables of interest are two scalar invariants of the velocity gradient tensor, called Q and R , defined by equations below:

$$Q(\mathbf{x}) = -\frac{1}{2}\text{Tr}[(\nabla \mathbf{u})^2] = \frac{1}{2}\omega^2 - S^2 \quad (4)$$

$$R(\mathbf{x}) = -\frac{1}{3}\text{Tr}[(\nabla \mathbf{u})^3] = -\det \nabla \mathbf{u} \quad (5)$$

In the flow, the above observables assume a range of values, with $S^2, \omega^2/2$ being non-negative while Q, R can be both positive or negative. Excursion sets are the set of points \mathbf{x} where such observables are above (or below) a certain threshold, for example $\omega^2/2 > \chi$ (χ will denote the threshold). We analyze the indicator function $\Theta_\chi(\mathbf{x})$ of the set of points which satisfy the stated condition. Given a set of interest associated with a threshold χ , we define its indicator function according to

$$\Theta_\chi(\mathbf{x}) = \begin{cases} 1, & \text{if } \mathbf{x} \in \text{set of interest associated with threshold } \chi \\ 0, & \text{otherwise} \end{cases} \quad (6)$$

An analogous definition can be made for ‘interval-based’ sets, for example, we can define the region where enstrophy assumes values between χ_- and χ_+ , i.e. $\chi_- < \omega^2/2 < \chi_+$. From here on, the latter regions will also be referred to as ‘iso-sets’, when χ_- and χ_+ are very close in value (small bin).

Various statistical features of these sets can be used to characterize their spatial distribution. We are especially interested in the two-point structure of these sets and thus focus on the correlation function of $\Theta_\chi(\mathbf{x})$ defined as:

$$\mathcal{C}_\chi(\mathbf{r}) = \langle \Theta_\chi(\mathbf{x}) \Theta_\chi(\mathbf{x} + \mathbf{r}) \rangle, \quad (7)$$

where the average is understood as a spatial average over positions \mathbf{x} when applied to statistically homogeneous flows. Note that we are not subtracting the averages of the indicator function (i.e. we do not define fluctuations of the indicator function but leave it as 0’s and 1’s).

In isotropic turbulence the more compact quantity is the angular average of the 3D correlation function:

$$C_\chi(r) = \frac{1}{\mathcal{C}_\chi(\mathbf{0})} \int_{S_2} \mathcal{C}_\chi(\mathbf{r}) d\Omega_{\mathbf{r}}, \quad (8)$$

i.e. the normalized, radial correlation function. Phenomenologically, one may expect power-law decaying behavior $C_\chi(r) \sim K_\chi r^{-\gamma_\chi}$ for r in the inertial range due to the expected self-similar behavior of turbulence in that range of scales. The power law exponent γ_χ is expected, however, to depend on the threshold. Writing the expected scaling behavior with its dimensional dependencies and a possibly Reynolds number and quantity-dependent prefactor K_χ , we write:

$$C_\chi(r) \sim K_\chi(\text{Re}_\lambda) \left(\frac{r}{\eta} \right)^{-\gamma_\chi}; \quad r \gg \eta, \quad r < L, \quad (9)$$

where η is the Kolmogorov scale and L the integral scale of the flow. The scaling exponent γ_χ is expected to be positive, consistent with a decay of the correlation at increasing distance. A more geometric interpretation of the exponent γ_χ can be invoked by recalling that the correlation dimension D is defined based on the scaling of the correlation function according to $C_\chi(r) \sim r^{D-E}$ [36] where E is the dimensionality of the embedding space (here $E = 3$). Thus the dimension corresponding to a correlation decay exponent γ_χ is $D(\chi) = 3 - \gamma_\chi$.

For this work, we chose to perform our analysis on a snapshot from the Johns Hopkins Turbulence Database. The data comes from a DNS of forced isotropic turbulence performance on a 1024^3 periodic grid, using a pseudo-spectral parallel code. The attained Taylor-scale based Reynolds number is $\text{Re}_\lambda \approx 433$ time averaged over the database time period, and $\text{Re}_\lambda \approx 426$ for the specific timestep used in the present analysis ($t = 0.0$). The domain is a periodic cube of size $[0, 2\pi]^3$, in which the data frames were stored after the simulation reached a statistically stationary state. Additional details of the dataset can be found in [31, 37]. In order to establish the scaling range corresponding to the turbulence inertial range for comparison with present results we evaluate the longitudinal structure function as an average over the three Cartesian directions:

$$D_{LL}(r) = \frac{1}{u_{rms}^2} \frac{1}{3} \sum_{i=0}^3 \langle (u_i(\mathbf{x} + r\mathbf{e}_i) - u_i(\mathbf{x}))^2 \rangle, \quad (10)$$

where \mathbf{e}_i is the unit vector in the direction of the velocity component u_i , and $u_{rms}^2 = \frac{1}{3} \sum_{i=0}^3 u_i^2$ is the square of the RMS velocity.

In order to evaluate enstrophy and dissipation, the velocity gradients are calculated with spectral accuracy using Fast Fourier Transform (FFT). For our present analysis we did not use the databases' finite differencing or Spline differencing tools since these are less accurate compared to spectral methods that were also used during the DNS. As further explained in Appendix A, the analysis was done on a server near the database using notebooks provided by a dedicated compute environment (the SciServer system). For differentiation, a 3D FFT operation is applied to the velocity field to obtain the velocity field in Fourier space, then the components are multiplied by the respective wavenumbers (ik_j) to obtain the velocity gradient in the x_j direction. Finally the inverse FFT is applied to obtain the velocity gradients in physical space. This allows us to obtain $A_{ij} = \partial_j u_i$ data from the velocity field \mathbf{u} . The observables we are interested in (dissipation S^2 , enstrophy $\omega^2/2$, Q and R) are then computed in physical space.

To compute the correlation functions efficiently in 3D, a 3D FFT is applied to $\Theta_\chi(\mathbf{x})$ over the 1024^3 data-cube, yielding $\hat{\Theta}_\chi(\mathbf{k})$ in Fourier space. To $\hat{\Theta}_\chi \hat{\Theta}_\chi^*$ is then applied the inverse Fourier transform, resulting in $\mathcal{C}(\mathbf{r})$, which is the full 3D two-point correlation function. The radial integration is done by evaluating a histogram based on the radial $\sqrt{|\mathbf{r}|^2}$ values computed over the resulting grid. This effectively performs the angular average by dividing the weighted average of the two-point correlation and the base $\sqrt{|\mathbf{r}|^2}$ histogram. More details are provided in Appendix A.

III. EXCURSION SET ANALYSIS

The excursion set indicator function for a given scalar field A , like enstrophy $A = \omega^2/2$ or dissipation $A = S^2$, is defined as:

$$\Theta_\chi^A(\mathbf{x}) = H(A(\mathbf{x}) - \chi) = \begin{cases} 1, & \text{if } A(\mathbf{x}) \geq \chi \\ 0, & \text{otherwise,} \end{cases} \quad (11)$$

where χ is the threshold applied on the scalar A . We begin by considering enstrophy excursion sets. Figure 1 shows a volume rendering of the scalar function corresponding to enstrophy above the threshold $\chi = 20\langle S^2 \rangle$, given by $\frac{1}{2}\omega_{ex}^2(\mathbf{x}) = \frac{1}{2}\omega^2(\mathbf{x})\Theta_{20\langle S^2 \rangle}(\mathbf{x})$. Note for consistency all threshold values are indicated as multiples of $\langle S^2 \rangle$ which is equally relevant to enstrophy here since in isotropic turbulence $\langle S^2 \rangle = \frac{1}{2}\langle \omega^2 \rangle$. As can be seen in Fig. 1(a), this set has a very rich structure with familiar elongated strong vortices visible.

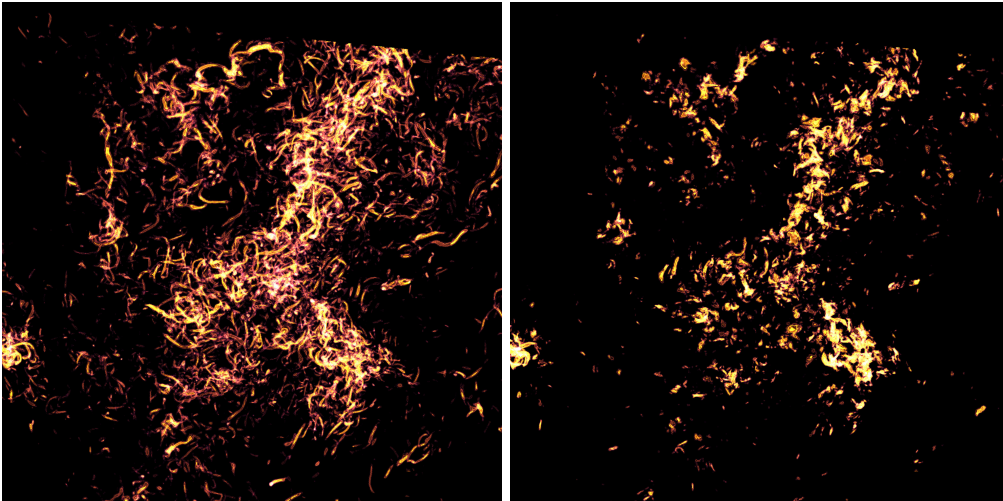


FIG. 1: Volume rendering of (a) the enstrophy excursion set corresponding to the function $\frac{1}{2}\omega_{ex}^2(\mathbf{x}) = \frac{1}{2}\omega^2(\mathbf{x})\Theta_{20\langle S^2 \rangle}^\omega(\mathbf{x})$ and (b) of dissipation excursion set corresponding to the function $S_{ex}^2(\mathbf{x}) = S^2(\mathbf{x})\Theta_{20\langle S^2 \rangle}^S(\mathbf{x})$ on a 512^3 subset of the full dataset, with $1/8$ in volume. The visualizations were generated using the YT-project python visualization library [38].

As a comparison, we also present in figure 1(b) the visualization of the dissipation field for the same threshold, i.e. $S_{ex}^2(\mathbf{x}) = S^2(\mathbf{x})\Theta_{20\langle S^2 \rangle}^S(\mathbf{x})$, which provides us with some useful insights. The most striking feature is that the overall geometric distribution of high intensity regions for dissipation closely follows the ones for high enstrophy, though the smaller scale details differ. The second feature is that at small-scales dissipation appears to be less 1-D like and more sheet like, but that when viewed at larger scales, in comparison to its enstrophy counterpart. As will be seen, this fact will be visible also quantitatively in the correlation function results.

A. Correlation function based scaling

The radial two-point correlation function of the enstrophy excursion set corresponding to $\chi = 20\langle S^2 \rangle$ is plotted in log-log axes in figure 2(a). A power-law tail is clearly visible over about a decade, between $42.5\eta < r < 425\eta$. This range corresponds, roughly, to inertial range of the studied dataset. For direct comparison, we computed the second-order structure functions for the dataset, as shown in figure 2(b). The structure function has a scaling exponent of about $\xi_2 = 0.68$ which is the known value (slightly above the K41 value of $2/3$ due to intermittency, [1]). These plots allow us to compare the quality and range of the power-laws found in both observables. The most important fact to notice is that the range where the two-point correlation function exhibits a near power-law behavior (the interval $42.5\eta < r < 425\eta$) is the same as in the structure function. A similar behavior will be observed for all the excursion, iso-sets, and joint distribution sets studied in this work.

The scaling exponent observed, in figure 2 for the enstrophy excursion set at the given threshold is about $\gamma_\chi \approx 0.766$, implying a ‘‘correlation dimension’’ of about $D(\chi) \approx 2.234$. Thus, while the topology of each individual vortex structure is visibly more one-dimensional, as a set its two-point structure is significantly more ‘‘space filling’’ with a correlation structure that decays more slowly on average than a collection of isolated vortices.

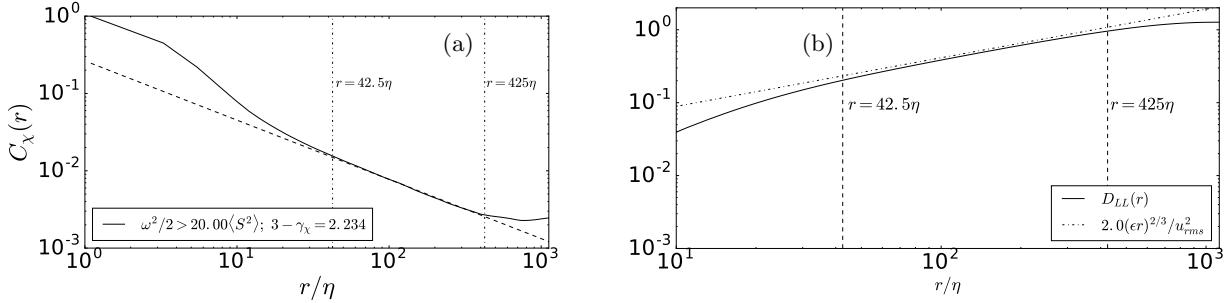


FIG. 2: (a): Radial two-point correlation function for the $\omega^2/2 > 20\langle S^2 \rangle$ excursion set. (b): Second-order longitudinal velocity structure function D_{LL} as function of distance r . The dotted line is the classical Kolmogorov prediction for the longitudinal 2nd-order structure function with $C_1 = 2.0$ (the small difference with the leading coefficient that is usually closer to $C_1 \approx 2.1$ can be attributed to statistical convergence since we are only using a single snapshot).

It is important to note that correlation functions were evaluated for the indicator function distribution directly (i.e. a field of ones and zeros), and not the ‘‘fluctuation’’ of the indicator function away from its spatial mean which would include negative values by necessity. We also tried to perform calculations on the subtracted version of the correlation function, but the resulting correlation functions do not present as clear a power-law behavior in the inertial range as the one without subtracting the mean. One plausibility argument for this observation is that the correlation function without subtracting the mean more readily corresponds to the definition of the mass dimension in which the mass in spheres of radius r is evaluated, and scaling with distance r is used to define the mass dimension [36]

B. Box-counting based dimensions

As an independent measure of fractal dimension for the excursion sets we can also compute the box-counting dimension and the box-counting based correlation dimension. The box-counting procedure for evaluating both of these dimensions is based on a set of cubes $B_{r,\mathbf{k}}$ of size r and location identified by indices

$\mathbf{k} = (k_1, k_2, k_3)$ so that a cube's corner is located at $[k_1 r, k_2 r, k_3 r]$ with $k_1, k_2, k_3 \in \mathbb{Z}$, and $0 \leq k_i \leq \lceil 2\pi/r \rceil$. We assign a measure to each cube, given by

$$\mu_\chi(B_{r,\mathbf{k}}) = \frac{1}{V_{2\pi}} \int_{B_{r,\mathbf{k}}} \Theta_\chi(\mathbf{x}) d^3 \mathbf{x}, \quad \text{where } V_{2\pi} = \int_{[0,2\pi]^3} \Theta_\chi(\mathbf{x}) d^3 \mathbf{x}. \quad (12)$$

The scaling of N_r , the number of boxes needed to cover the set, and of $\sum_{\mathbf{k}} \mu_\chi(B_{r,\mathbf{k}})^2$ is used to define the box-counting dimension and the box-counting based correlation dimension, respectively. We thus compute

$$N_r = \sum_{\mathbf{k}} [\mu_\chi(B_{r,\mathbf{k}})]^0, \quad \text{where } \mu_\chi(B_{r,\mathbf{k}})^0 = \begin{cases} 1, & \text{if } \int_{B_{r,\mathbf{k}}} \Theta_\chi(\mathbf{x}) d^3 \mathbf{x} > 0 \\ 0, & \text{otherwise} \end{cases} \quad (13)$$

as well as

$$\mathcal{M}_2(r) = \sum_{\mathbf{k}} [\mu_\chi(B_{r,\mathbf{k}})]^2. \quad (14)$$

The behavior $N_r \sim (r/\eta)^{-D_0}$ defines the box-counting dimension D_0 , and $\mathcal{M}_2(r) \sim (r/\eta)^{D_2}$ defines the box-counting based correlation dimension, D_2 [13, 39].

The implementation of the box-counting dimension is done as follows: The positions of all points in the set are histogrammed using the cubic box boundaries as the bins boundaries. For each bin with non-zero count, the bin was normalized to 1, and all other bins are left to 0. The resulting histogram is summed, yielding the number of boxes that intersect the set of interest, N_r . The box size r ranges between 4.25η and 850η . For the box-counting based correlation dimension, the computation is similar, but instead of normalizing the resulting count, we compute the sum of the bin values squared, which amounts to the $\mu_\chi(B_{r,k})^2$ calculation.

The results for the box-counting dimension can be seen in Fig. 3(a) and the box-counting based correlation dimension plot is presented in Fig. 3(b). The most notable feature of both plots is the lack of an inertial range scaling behavior, in contrast with the structure function and the correlation dimension for the same set, Fig. 2(a). One can discern a scaling at small scales $r < 20\eta$ in Fig. 3(a) with a slope near -1 which implies $D_0 \sim 1$, i.e. 1-D objects, not unexpected for vortices at the viscous scales. However, no scaling is observed in the inertial range with smooth curving towards a slope of -3 (space-filling) at larger scales $r > 200\eta$ approaching the integral scale. Similar conclusions are reached from the plots in Fig. 3(b). Hence, no inertial-range power-law scaling is found for the box-counting approach applied to the excursion set of enstrophy. We have verified that the same is true for dissipation and all other variables considered in this paper (not shown but some limited results will be shown later). Hence, we focus our further analysis on the correlation-function based analysis and scaling. We have tested that the correlation and box-counting algorithms yield correct results based on a 3D fractal set of known dimension (the Menger sponge), as summarized in Appendix B.

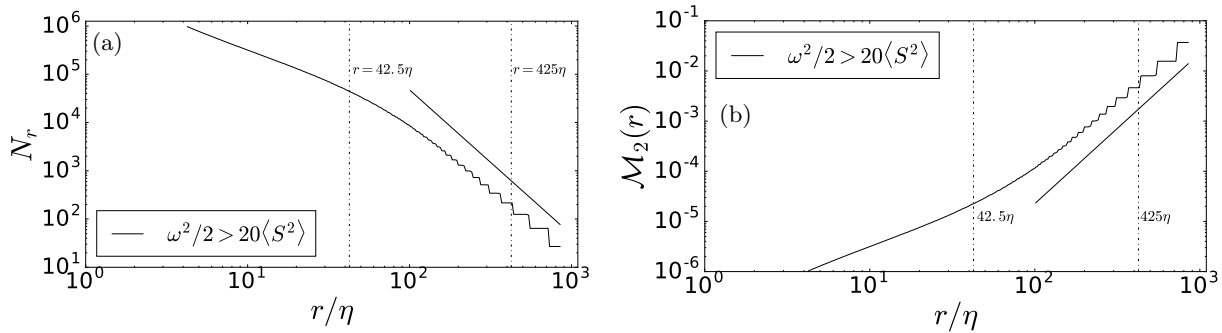


FIG. 3: (a): Box-counting dimension plot for the enstrophy excursion set with threshold $\chi = 20\langle S^2 \rangle$. (b): Box-counting based correlation dimension plot for the same set. The black line represents the $D_0 = D_2 \sim 3$ scaling expected for the large scales of the box-counting calculation, since at large scales the clusters appear space-filling.

C. Dependence on threshold, and dissipation-based excursion sets

In this section we examine the correlation function scaling as a function of threshold and also present a similar analysis for the dissipation S^2 . To place the thresholds in proper context, in figure (4) we present the probability density function (PDF) for both enstrophy and dissipation, together with their joint PDF, for the dataset we used. Varying the threshold χ we can probe different intensities of events, therefore different sectors of the PDFs. We present, in figure (5), the results for the correlation functions for several thresholds, ranging from $\chi = 1\langle S^2 \rangle$ to $\chi = 50\langle S^2 \rangle$, for both enstrophy (see Figs. 5(a,b)) and for dissipation (Fig. 5(c,d)).

Clearly all correlation functions shown in Figure 5 present power-law behavior within the inertial range regardless of the observable probed and the value of the threshold. As expected, the correlation dimension has a monotonically decreasing behavior as a function of the threshold, indicating that high intensity sets become less and less space filling.

Comparing the values presented in Figures 5(a,c) with 5(b,d) confirms the initial observations made about figure 1, in which is clear that the fractal dimensions associated with dissipation sets are systematically lower than the ones of the enstrophy sets, for the same thresholding value.

This behavior is, initially, counterintuitive due to the expectation that enstrophy should be distributed along tubes, i.e. elongated one-dimensional sets, while dissipation should be distributed along sheets. This behavior is expected on the smallest, viscous, scales but does not seem not to be reflected in the inertial range behaviour, at least not in the correlation function scaling.

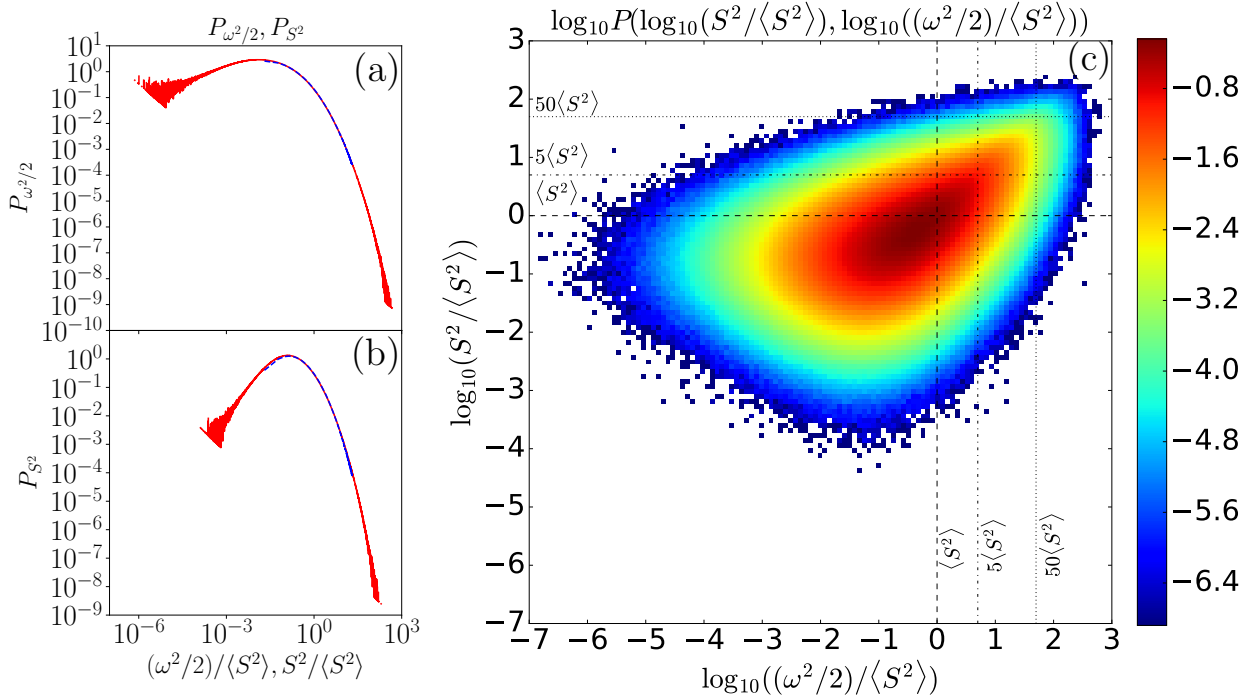


FIG. 4: (a) Enstrophy and (b) Dissipation PDFs, computed from DNS of forced isotropic turbulence at $Re_\lambda \sim 430$. The dashed blue line is the same PDF computed using a different analysis program for this same dataset as reported in Ref. [40]. (c) Enstrophy and Dissipation Joint-PDF. A similar joint PDF can be found in reference [41].

Another feature visible in by Fig. 1 is that enstrophy and strainrate are quite highly correlated, which can also be inferred from the overall shape of the joint PDF shown in Fig. (4)(c). Quantitatively, we confirmed this by computing the correlation coefficients as follows:

$$\rho(S^2, \omega^2/2) = \frac{\langle (S^2 - \langle S^2 \rangle)(\omega^2/2 - \langle \omega^2/2 \rangle) \rangle}{\langle (S^2 - \langle S^2 \rangle)^2 \rangle^{1/2} \langle (\omega^2/2 - \langle \omega^2/2 \rangle)^2 \rangle^{1/2}} = 0.615. \quad (15)$$

$$\rho(\log S^2, \log \omega^2/2) = \frac{\langle (\log S^2/\langle S^2 \rangle)(\log \omega^2/2/\langle \omega^2/2 \rangle) \rangle}{\langle (\log S^2/\langle S^2 \rangle)^2 \rangle^{1/2} \langle (\log \omega^2/2/\langle \omega^2/2 \rangle)^2 \rangle^{1/2}} = 0.675. \quad (16)$$

The non-negligible correlation between enstrophy and dissipation has been noted before, see, e.g. [33–35].

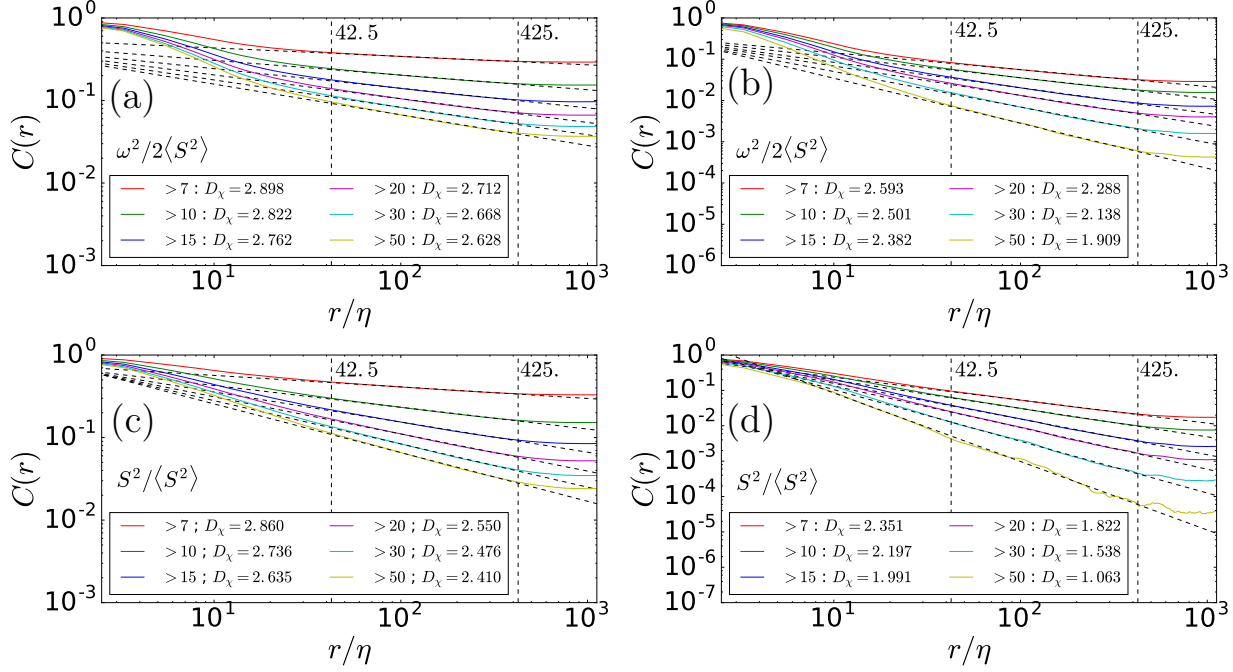


FIG. 5: Radial correlation functions for enstrophy $\omega^2/2$ (a,b) and dissipation S^2 (c,d) computed from DNS of forced isotropic turbulence at $Re_\lambda \sim 430$. The thresholds χ range from $1\langle S^2 \rangle$ to $50\langle S^2 \rangle$. The legend denotes $> \chi/\langle S^2 \rangle$ threshold for each line.

For comparison we present, in Figure 6, the box-counting dimension for these same sets, based on thresholding enstrophy and dissipation. They present the same features as in figure 3(a,b). At the smallest scales we can see that most high-enstrophy sets approach a slope of -1 but very high thresholds lead to even shallower (smaller-in-magnitude) slopes, consistent with broken up, less coherent vortex events. For the dissipation structures, at small scales we see a range of slopes between -2 for intermediate thresholds (consistent with sheets) but also decreasing continuously towards -1 and lower for higher thresholds. For the larger scales we notice again that all excursion sets saturate the box-counting to a slope of ~ -3 due to the homogeneity (space-fillingness) of the turbulence structures at the largest scales.

The lack of scaling of the box-counting results in the inertial range makes connection of the correlation function based exponent $D(\chi) = 3 - \gamma_\chi$ with a fractal dimension not as clear as one would hope. Therefore, while from here on we will refer to $D(\chi) = 3 - \gamma_\chi$ as the correlation dimension, we must keep these limitations in mind.

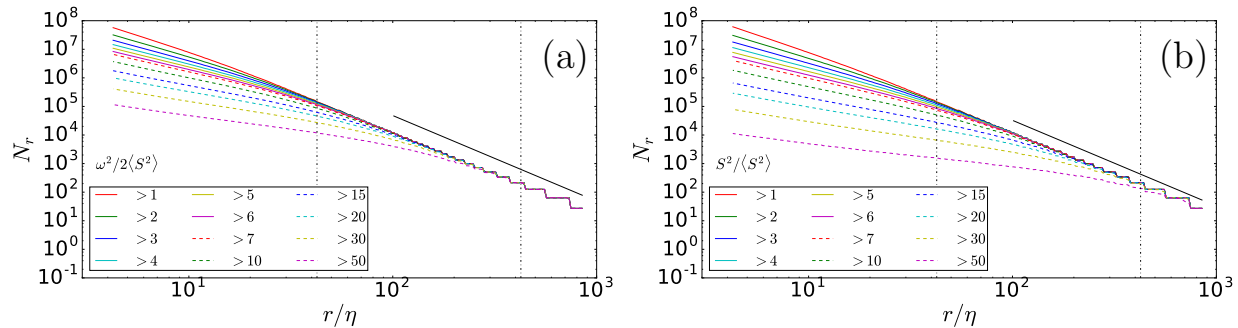


FIG. 6: Box-counting dimension calculation for enstrophy (a) and dissipation (b) excursion sets showing lack of power-law scaling in the inertial range. The black line represents the $D_0 = 3$ scaling expected for the large scales. The legend denotes $> \chi/\langle S^2 \rangle$ threshold for each line.

IV. INTERVAL-BASED (ISO) SETS

An interesting alternative to considering excursion sets is to compute interval-based sets, which corresponds to the sets in which the observable is between χ_- and χ_+ , a lower and a upper threshold respectively. These sets are defined according to

$$\Theta_{\chi_+, \chi_-}^A(\mathbf{x}) = H(A(\mathbf{x}) - \chi_-)H(\chi_+ - A(\mathbf{x})) = \begin{cases} 1, & \text{if } \chi_- \leq A(\mathbf{x}) \leq \chi_+ \\ 0, & \text{otherwise} \end{cases} \quad (17)$$

They correspond to subsets of the excursion set near the lowest threshold, i.e. near the iso-threshold set bounding the excursion set. In fact this procedure yields a good approximation for an ‘‘iso-set’’ when $(\chi_+ - \chi_-)/\chi_- \ll 1$.

We compute the two-point correlation function using χ_- varying in the same set as the thresholds of the previous section, and $\chi_+ = 1.05\chi_- = (1 + \Delta)\chi_-$, which roughly corresponds to a thin shell of the inner boundary of the excursion set of threshold χ_- . We prefer a multiplicative, rather than additive, relationship between χ_+ and χ_- because it amounts to equally sized logarithmic bins. We also refer to these ‘‘interval-based’’ sets as ‘‘shells’’ sets.

The results of this analysis are presented in figure 7(a,b) for enstrophy and in figures 7(c,d) for dissipation. As is visible, the resulting two-point correlations also present robust power-law scaling in the same inertial range as the previous excursion set correlation functions.

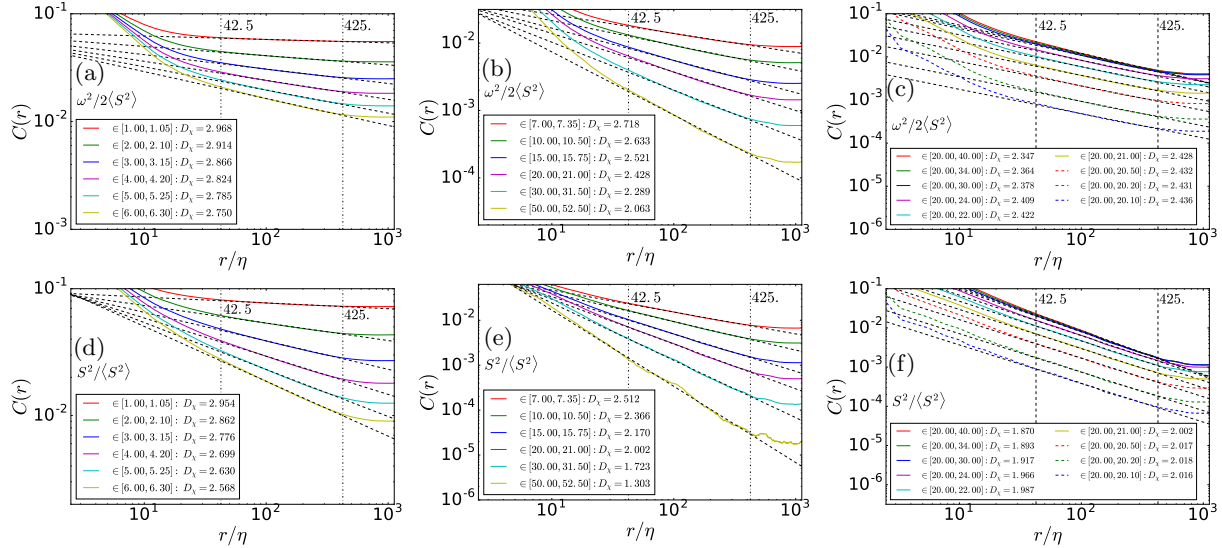


FIG. 7: Radial correlation functions for enstrophy $\omega^2/2$ and dissipation S^2 computed from DNS of forced isotropic turbulence at $Re_\lambda \sim 430$. The thresholds χ range from $1\langle S^2 \rangle$ to $50\langle S^2 \rangle$. The results are for shells of thickness $\chi_+ - \chi_- = 0.05\chi_-$, for both enstrophy, (a) and (b), and for dissipation, (d) and (e). As a band-width sensitivity test, we computed correlation functions for shells of varying thickness with base threshold $\chi_- = 20\langle S^2 \rangle$, for both enstrophy (c) and dissipation (f). Legend denotes $\in [\chi_-/\langle S^2 \rangle, \chi_+/\langle S^2 \rangle]$ interval for each observable.

In order to establish the robustness of results with regards to the ‘‘thickness’’ of the band of thresholds defining the bin for the iso-set, we computed correlation functions for shells of varying thickness with base threshold $\chi_- = 20\langle S^2 \rangle$, for both enstrophy and dissipation. As can be seen in Fig. 7(c) for enstrophy, the resulting power-law can be observed to be robust regardless of the tested thickness. Also, the resulting exponent is insensitive to the thickness, unless very thick shells are used, in which case we are actually closer to an excursion set than to a proper interval-based (iso) set. A similar result can be obtained for the dissipation, as seen in Fig. 7(f). Again, we repeated the box-counting dimensions computation for reference (not shown), and observed that there is no power-law in the inertial range.

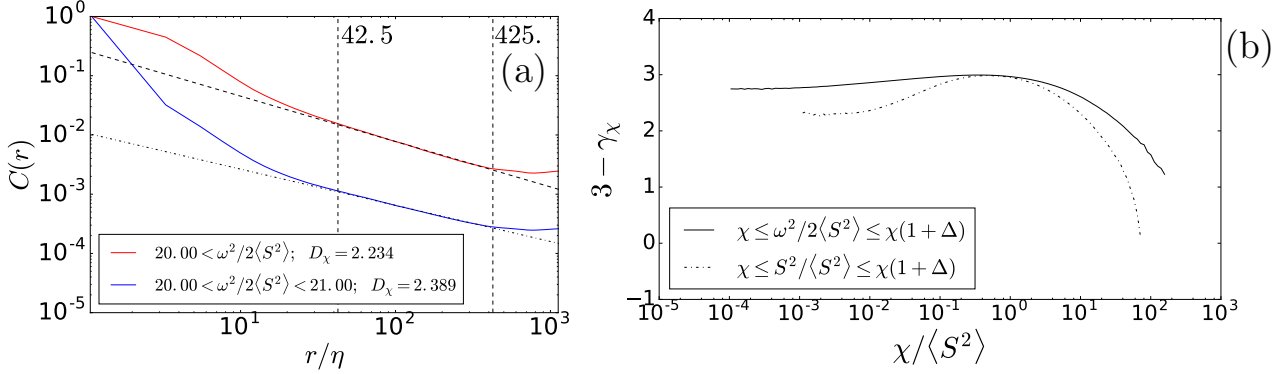


FIG. 8: (a) Comparison of excursion sets with thin shell sets starting at similar threshold values; (b) Interval-based sets dimensions, as a function of the probed intensity $\chi/\langle S^2 \rangle$.

To exemplify the difference in behavior between excursion sets and interval-based sets correlation functions, we computed both types of sets for the lower threshold at $20\langle S^2 \rangle$ in both cases. One observes that they differ, mostly, on the small r region, which is an imprint of the fact that shell-based sets have a “hollow” shape compared to the excursion sets. The absolute value of the normalized correlation function is lower for shells than for the respective excursion sets, due to lower volume fraction, as expected. The correlation slope is flatter, having a higher compensated exponent (i.e. more “space-filling”).

In order to present the complete information of scaling exponents as function of threshold we present $D(\chi) = 3 - \gamma_\chi$ as function of threshold corresponding to logarithmically spaced bins. The computation is done for both enstrophy and dissipation shell sets. Overall both observables present the same qualitative behavior, but enstrophy consistently shows a higher correlation-based dimension. Prior results [29] have shown that enstrophy is “more intermittent” than dissipation and thus the present results may appear to be counterintuitive, as mentioned before in section III. Present results show is that the decay of spatial correlation is slower with distance for the high enstrophy region as compared to the high dissipation regions which must be more “broken up” and less coherent, consistent with what is seen in the visualization, Fig. 1(b). We conjecture that the slow correlation decay reflects the underlying highly elongated structure of high vorticity regions, which is not the same for most of the other observables.

V. JOINT ISO-SET ANALYSIS

As done for a single scalar, it is possible to define joint excursion sets for both enstrophy $\omega^2/2$ and dissipation $S^2 = S_{ij}S_{ij}$, according to:

$$\begin{aligned} \Theta_{\chi_\omega, \chi_\epsilon}^{\omega\epsilon}(\mathbf{x}) &= \Theta(\omega^2/2 - \chi_\omega)\Theta(S^2 - \chi_\epsilon) \\ &= \begin{cases} 1, & \text{if } \omega^2 \geq \chi_\omega \text{ and } S^2 \geq \chi_\epsilon \\ 0, & \text{otherwise} \end{cases} \end{aligned} \quad (18)$$

The radial correlation function of these sets are computed following the same approach as in the previous section (§III). Representative results are shown in figures 9(a,b). We observe the same overall power-law behavior seen in the single excursion sets, in the same range of length-scales corresponding to the inertial range. Similarly, we can define joint interval-based sets according to

$$\begin{aligned} \Theta_{\chi_\omega, \chi_\epsilon, \Delta}^{\omega\epsilon}(\mathbf{x}) &= \Theta(\omega^2/2 - \chi_\omega)\Theta(\chi_\omega(1 + \Delta_\omega) - \omega^2/2)\Theta(S^2 - \chi_\epsilon)\Theta(\chi_\epsilon(1 + \Delta_\epsilon) - S^2) \\ &= \begin{cases} 1, & \text{if } \chi_\omega \leq \omega^2/2 \leq \chi_\omega(1 + \Delta_\omega) \text{ and } \chi_\epsilon \leq S^2 \leq \chi_\epsilon(1 + \Delta_\epsilon) \\ 0, & \text{otherwise} \end{cases} \end{aligned} \quad (19)$$

For very small spacings Δ , there might be numerical and statistical problems due to the very small number of points on a finite dataset. Therefore, the map of the joint 2-point correlation function is only accurate for the center most region, away from the skirt of the joint probability distribution function, in figure (10).

Though not shown here, we also performed sensitivity analysis to the bin size, analogously to the presented in figure 7(c,f), and similar results were obtained.

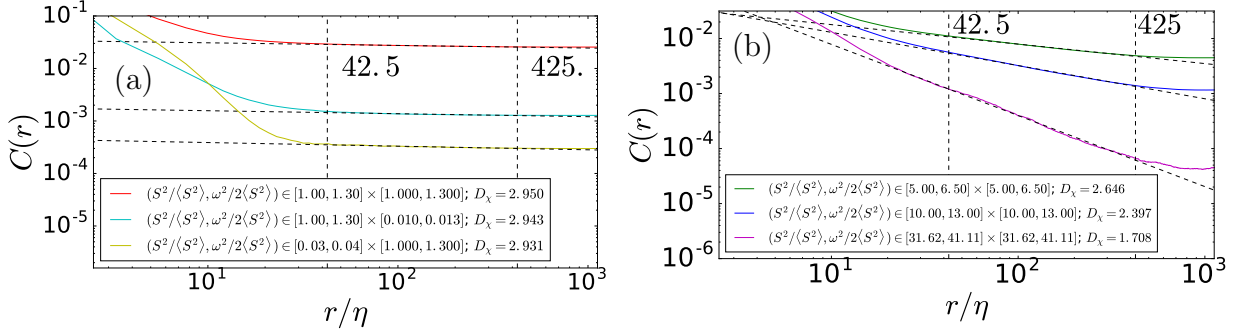


FIG. 9: Set of representative log-log plots showing power law scaling of the correlation functions for joint shell sets on enstrophy $\omega^2/2$ and dissipation S^2

One feature we observe in figure (10) is the presence of an inverted/rotated “L-shaped” region of constant dimension, indicating a near independence of the geometrical distribution of one of the observables. This indicates that the regions with either average enstrophy or dissipation are dominated by space-filling geometry, irrespective of the value of the other quantity within those regions. As regions of very high or very low enstrophy and dissipation are probed, we observe lower and lower correlation dimension $D(\chi_\omega, \chi_\epsilon) = 3 - \gamma_{\chi_\omega, \chi_\epsilon}$, as expected. The lowest observed compensated exponent on the probed region is around $D(\chi_\omega, \chi_\epsilon) \approx 1.2$.

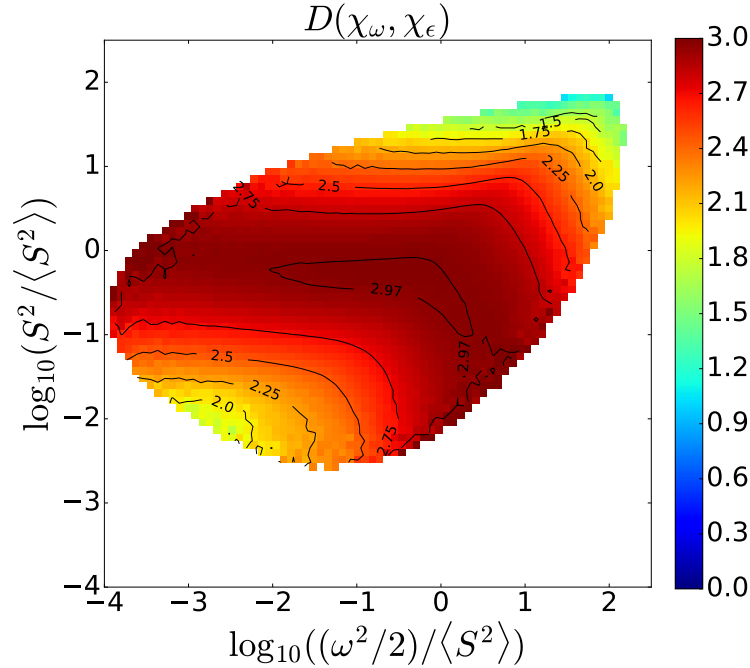


FIG. 10: Joint correlation function exponent $D(\chi_\omega, \chi_\epsilon) = 3 - \gamma_{\chi_\omega, \chi_\epsilon}$ for joint interval-based sets, with equally spaced logarithmic bins $\Delta = \Delta_\omega = \Delta_\epsilon \approx 0.28$, with the same χ_ϵ bins utilized to compute the joint-PDF in figure (4c).

Considering the values along the diagonal where $S^2 = \omega^2/2$, or $Q = 0$, i.e. $D_{\text{diag}}(\chi) = D(\chi, \chi)$, we can approximate the joint distribution only in terms of this function, i.e. $D(\chi_\omega, \chi_\epsilon) \approx D_{\text{diag}}(\max\{\chi_\omega, \chi_\epsilon\})$. This approximation reproduces the L-shaped pattern quite well (not shown), suggesting that any $Q \neq 0$ regions have, to a first approximation, the dimension associated with the $Q = 0$ hull for the component with the highest intensity, of either S^2 or $\omega^2/2$.

VI. SCALING ANALYSIS OF SPATIAL DISTRIBUTION OF INVARIANTS Q AND R :

Following the work done in the previous sections, we seek to probe the geometrical structure of the observables Q and R defined in equation (4). Since both quantities are signed, we computed their PDFs as function of thresholds in linear instead of logarithmic scale. First, we present the PDFs of both quantities, in Fig. 13(a,b), and the joint PDF of Q and R in Fig 13(c). We notice the characteristic tear-drop shape in the joint PDF, with the right-most region following the so called Vieillefosse tail as $Q = -\frac{3}{2^{3/2}}R^{2/3}$. More details can be found in Refs. [42–45].

The quantities in Fig. 13(a,b) were plotted on inverse hyperbolic sine (asinh) axis. The asymptotic behavior of asinh for large values is to approach log, while being linear close to the origin. These features allow us to have a reasonably undistorted view of the PDF near the origin, and also verify if there is any power law behavior on the tails of the PDF, for either positive or negative values of the quantities of interest. In this case it appears that no power-law behavior is visible in the tails of the PDFs of Q and R , on either positive or negative sides.

Before proceeding to analyze the spatial correlation functions of the corresponding shell sets, it is useful to present visualizations of the Q and R scalar fields. In figure 11 we observe that the overall, middle and large scale spatial distribution strongly resembles the ones present earlier in figure 1, especially comparing Fig. 1(a) and Fig. 11(b). This resemblance is expected since $Q > 0$ thresholds are often used as vortex visualizations (the Q -criterion [46]). Negative Q regions are more correlated with high straining region, again as expected based on the identity $Q = \omega^2/2 - S^2$.

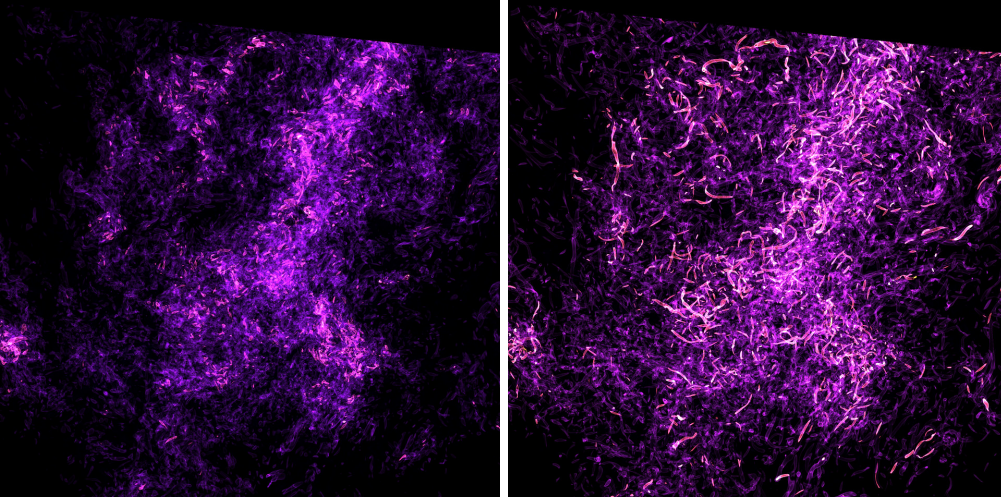


FIG. 11: Volume rendering of (a) the Q velocity gradient invariant excursion set for negative $Q < -2\langle S^2 \rangle$, i.e. corresponding to the function $Q_{ex}(\mathbf{x}) = -Q(\mathbf{x})\Theta_{2\langle S^2 \rangle}^{-Q}(\mathbf{x})$ and (b) the Q excursion set for positive $Q > 2\langle S^2 \rangle$, i.e. corresponding to the function $Q_{ex}(\mathbf{x}) = Q(\mathbf{x})\Theta_{2\langle S^2 \rangle}^Q(\mathbf{x})$ on a 512^3 subset of the full data.

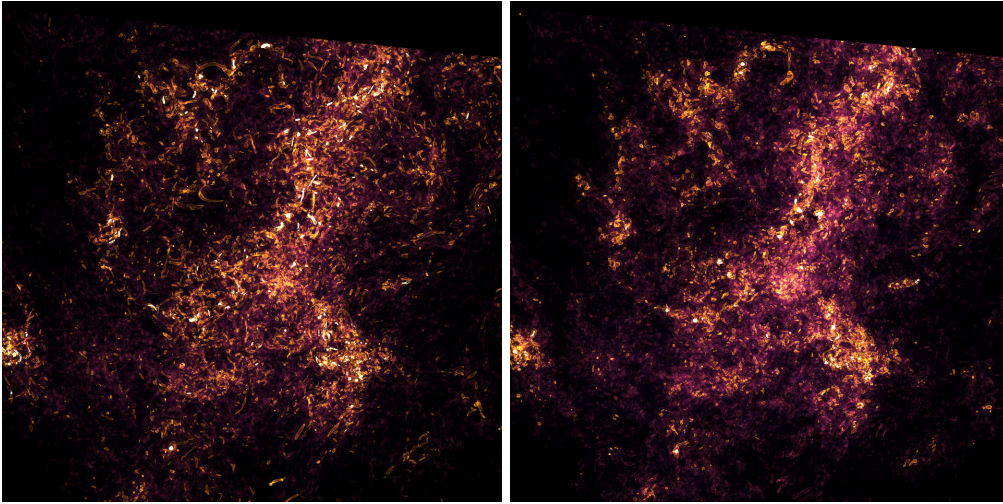


FIG. 12: Volume rendering of (a) the R velocity gradient invariant excursion set corresponding to the function $R_{ex}(\mathbf{x}) = -R(\mathbf{x})\Theta_{2(S^2)}^{-R}(\mathbf{x})$ and (b) of R set corresponding to the function $R_{ex}(\mathbf{x}) = R(\mathbf{x})\Theta_{2(S^2)}^R(\mathbf{x})$ on a subset of the full cube, with $1/8$ in volume.

Visualizations of spatial distributions of the scalar R are less common in the literature (although see discussion in Ref. [47]). Interestingly, we observe that negative R , in figure 12(a), include slightly more elongated structures than the positive R distributions, Fig. 12(b). Hence, the regions in which both Q and R show elongated structures are in the upper-left quadrant of the RQ plane, the vortex stretching quadrant.

To quantify the spatial correlation structure, the correlation functions of interval-sets are computed as before, for various thresholds of Q and R . Similarly to what is observed for enstrophy and dissipation, we find clear power-laws in the two-point correlation functions associated with the iso-sets of Q and R , as exemplified in figure 14(a).

The measured correlation dimensions, as a function of the threshold χ , are presented in figure Fig. (14b). The basic behavior of the correlation dimension mimics the PDF of the corresponding observable, as can be seen comparing 13(a,b) and 14(b).

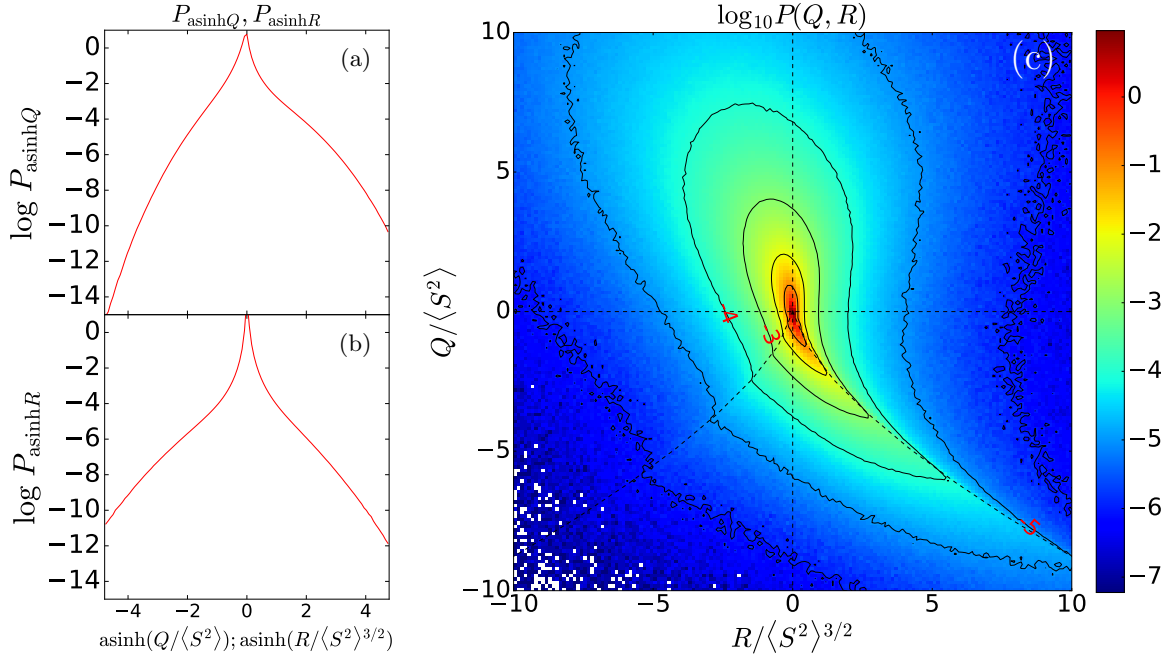


FIG. 13: PDFs of Q (a) and R (b) PDFs. (c) Q and R Joint-PDF, a similar joint PDF can be seen in reference [43].

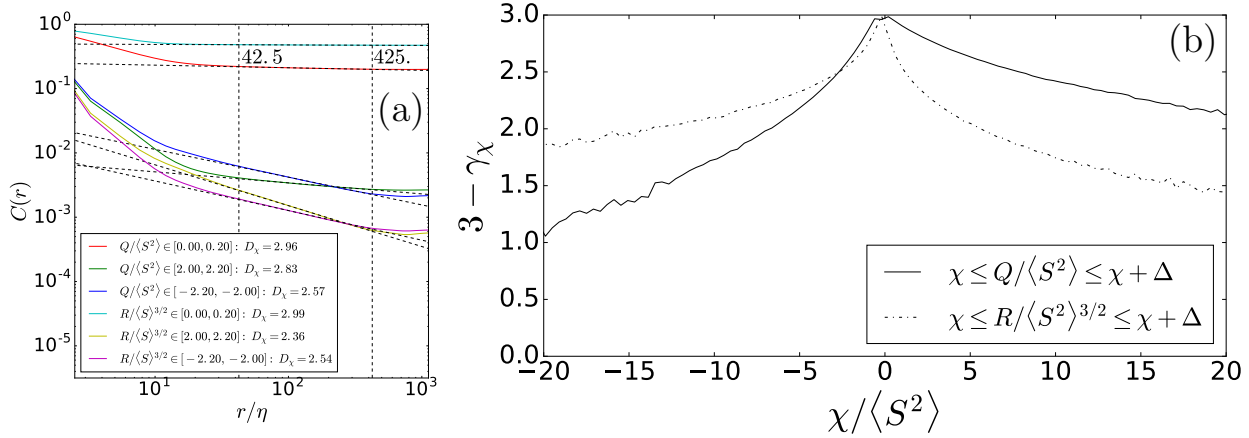


FIG. 14: (a): Correlation functions for selected values of Q and R . (b): Correlation-based dimensions of joint interval-based sets, as a function of thresholds on Q and R .

For the analysis of joint Q and R sets, we present some representative log-log plots in Fig. 15(a,b), which showcase that the correlation function presents power-law behavior for these sets as well. The full joint correlation dimension distribution is presented in Fig. 16.

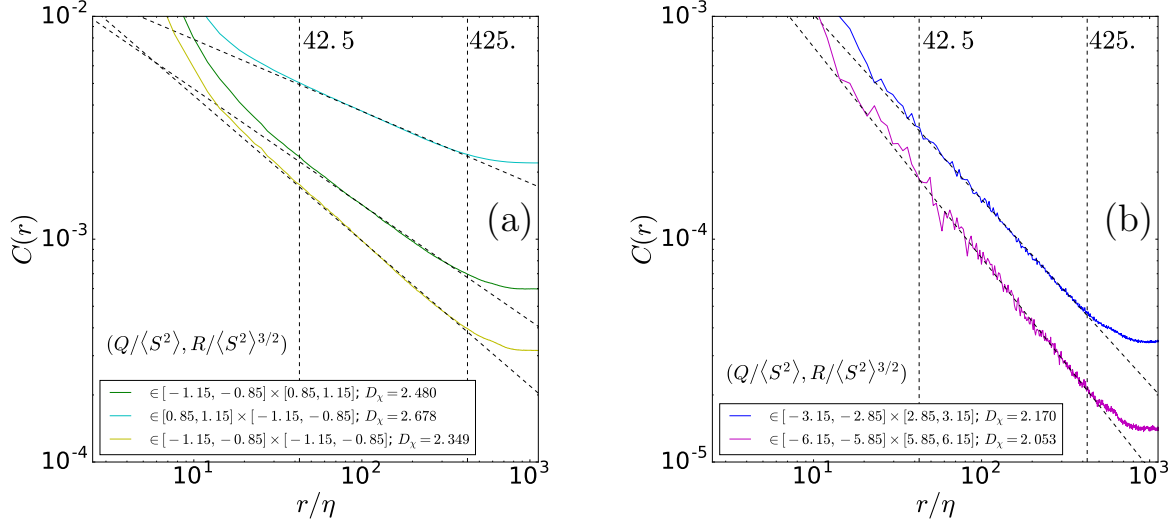


FIG. 15: Set of representative log-log plots for power law of the correlation functions for joint shell sets for Q and R velocity gradient invariants

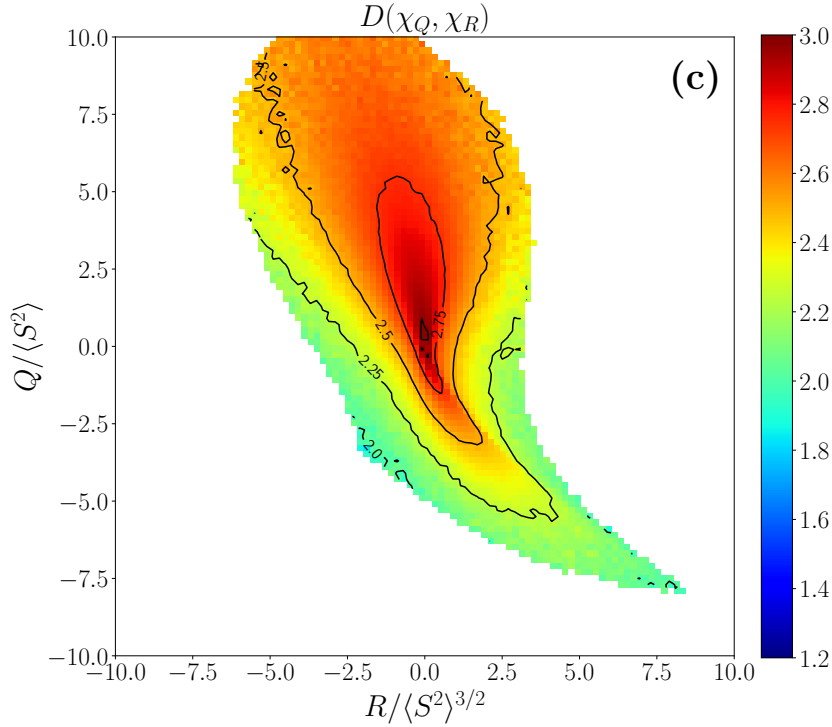


FIG. 16: Joint correlation function exponent $D(\chi_\omega, \chi_\epsilon) = 3 - \gamma_{\chi_Q, \chi_R}$ for joint interval-based sets, with equally spaced linear bins $\Delta = \Delta_Q = \Delta_R = 0.2$.

The most striking feature of Fig. (16) is the top-bottom asymmetry of the $Q > 0$ and $Q < 0$ regions for the correlation-based dimension. The dimension is clearly larger in the rotation dominated regions at $Q > 0$. This is consistent with the fact that, for the same threshold, correlation dimensions associated with enstrophy iso-sets are higher than dissipation iso-sets (Fig. 8(b)). Clearly the geometric features of the joint distribution differs from the joint PDF in Fig. 13(c). That is to say, regions with high PDF need not have higher (more space-filling) correlation-based dimension.

VII. CONCLUSIONS

We have analyzed a turbulence dataset from DNS at a moderately high Reynolds number, with the specific aim to identify scaling laws characterizing the spatial distribution of phenomena of various magnitudes. Both excursion sets and iso-sets (thin bands) have been considered for the enstrophy, dissipation (or square-strain-rate), and the two invariants Q and R . The variable Q has also often been used for flow visualization and high positive values of Q can be used to identify vortices. The spatial distributions are first defined using an indicator function and the radial correlation function of the indicator function distribution is evaluated. In all cases we find clear power-law decay in these correlations for separation distances falling within the inertial range of turbulence. The scaling range is insensitive to the thresholds and variable of interest. We confirmed this is the same scaling range characterizing power-law scaling of the traditional velocity structure function.

Even though the correlation functions present power-law in the inertial range, no such power-law behavior is observed in box-counting and box-counting based correlation dimension computations. Thus the interpretation of the correlation-function based exponents $D(\chi) = 3 - \gamma$ as a “dimension” must be considered with care. Consistent with the definition of a dimension, for thresholds near the mean value, space fillingness is observed with the exponent saturating at 3. For higher (or lower) thresholds, this correlation dimension reduces to lower values.

We also observe some surprising trends, such as a lower correlation-function based dimension for strong dissipation events compared to strong enstrophy events. It is likely that this is caused by the elongated nature of vortices causing coherence in space over longer distances on average as compared to regions of high dissipation. We also show that sets defined by joint conditions on strain and enstrophy, and on Q and R , also display power law scaling in the correlation functions, providing further characterization of the complex spatial structure of the intersections of these sets.

The inertial range power-law behavior of correlation functions associated with quantities in the viscous range (dissipation, enstrophy, Q and R) of a wide range of thresholds provides further evidence of geometric self similarity of flow properties in the inertial range

Overall, this work shows an alternate route to study multifractal behavior of turbulence, in which geometrical information is probed explicitly by using correlation functions of indicator functions. It is not yet immediately clear how to naturally connect the results of the present work with the traditional multi-fractal formalism, which is based on the scaling of statistical high-order moments of the box-averaged flow quantities over regions of different sizes. Specifically, it is not clear how to associate the threshold χ to the parameters α or h used in the multifractal formalism.

Further followup work should develop such correspondences, as well as examine the scaling for different (higher) Reynolds numbers. Also, extensions to non-isotropic shear flows, in which the correlation functions may decay differently in different directions, would be of interest.

Acknowledgements

The authors are grateful to the Turbulence Research Group members for discussions and help with this project, Dr. Gerard Lemson and Dr. Stephen Hamilton for their help with the SciServer system. José Hugo Elsas is grateful to the Rio de Janeiro state science funding agency FAPERJ program for international Ph.D. exchange, grant number E-26/200.076/2016 and to Dr. L. Moriconi for authorizing the international exchange. Alexander Szalay and Charles Meneveau are supported by NSF’s CDS&E: CBET-1507469 and BigData:OCE-1633124 projects. The SciServer project is supported by NSF’s DIBBS program (OAC-1261715).

SciServer is a collaborative research environment for large-scale data-driven science. It is being developed at, and administered by, the Institute for Data Intensive Engineering and Science at Johns Hopkins University. SciServer is funded by the National Science Foundation Award ACI-1261715. For more information about SciServer, please visit <http://www.sciserver.org>.

[1] U. Frisch. *Turbulence. The legacy of A. N. Kolmogorov*. 1995.

[2] A. N. Kolmogorov. The local structure of turbulence in incompressible viscous fluid for very large reynolds numbers. *Proceedings of the USSR Academy of Sciences*, 30:299303, 1941.

- [3] A. N. Kolmogorov. A refinement of previous hypotheses concerning the local structure of turbulence in a viscous incompressible fluid at high reynolds number. *Journal of Fluid Mechanics*, 13(1):8285, 1962. doi: 10.1017/S0022112062000518.
- [4] A. M. Oboukhov. Some specific features of atmospheric turbulence. *Journal of Fluid Mechanics*, 13(1):7781, 1962. doi: 10.1017/S0022112062000506.
- [5] A. A. Novikov and R. W. Stewart. Intermittency of turbulence and the spectrum of fluctuations of energy dissipation. *Izv. Akad. Nauk. SSSR, Geofiz.*, 3:408, 1964.
- [6] E. A. Novikov. Scale Similarity for Random Fields. *Soviet Physics Doklady*, 14:104, August 1969.
- [7] E. A. Novikov. Intermittency and scale similarity in the structure of a turbulent flow. *Prikl. Mat. Mech.*, 35: 266–277, 1971.
- [8] E. A. Novikov. The effects of intermittency on statistical characteristics of turbulence and scale similarity of breakdown coefficients. *Physics of Fluids A: Fluid Dynamics*, 2(5):814–820, 1990. doi: 10.1063/1.857629. URL <http://dx.doi.org/10.1063/1.857629>.
- [9] B. B. Mandelbrot. Intermittent turbulence in self-similar cascades: divergence of high moments and dimension of the carrier. *Journal of Fluid Mechanics*, 62(2):331358, 1974. doi: 10.1017/S0022112074000711.
- [10] U. Frisch, P. L. Sulem, and M. Nelkin. A simple dynamical model of intermittent fully developed turbulence. *Journal of Fluid Mechanics*, 87(4):719736, 1978. doi: 10.1017/S0022112078001846.
- [11] R. Benzi, G. Paladin, G. Parisi, and A. Vulpiani. On the multifractal nature of fully developed turbulence and chaotic systems. *Journal of Physics A: Mathematical and General*, 17(18):3521, 1984. URL <http://stacks.iop.org/0305-4470/17/i=18/a=021>.
- [12] C. Meneveau and K. R. Sreenivasan. Simple multifractal cascade model for fully developed turbulence. *Phys. Rev. Lett.*, 59:1424–1427, Sep 1987.
- [13] C. Meneveau and K. R. Sreenivasan. The multifractal nature of turbulent energy dissipation. *Journal of Fluid Mechanics*, 224:429484, 1991.
- [14] U. Frisch and G. Parisi. On the singularity structure of fully developed turbulence.
- [15] K. R. Sreenivasan. Fractals and multifractals in fluid turbulence. *Annual Review of Fluid Mechanics*, 23(1): 539–604, 1991.
- [16] T. Ishihara, T. Gotoh, and Y. Kaneda. Study of high–reynolds number isotropic turbulence by direct numerical simulation. *Annual Review of Fluid Mechanics*, 41:165–180, 2009.
- [17] T. Ishihara and H. Higuchi. *Multifractal Analysis by Using High-Resolution Direct Numerical Simulation of Turbulence*, pages 61–66. Springer Netherlands, Dordrecht, 2008.
- [18] C. Meneveau and J. O’Neil. Scaling laws of the dissipation rate of turbulent subgrid-scale kinetic energy. *Phys. Rev. E*, 49:2866–2874, Apr 1994.
- [19] L. Biferale, E. Calzavarini, and F. Toschi. Multi-time multi-scale correlation functions in hydrodynamic turbulence. *Physics of Fluids*, 23(8):085107, 2011. doi: 10.1063/1.3623466.
- [20] R. Benzi, S. Ciliberto, R. Tripiccion, C. Baudet, F. Massaioli, and S. Succi. Extended self-similarity in turbulent flows. *Phys. Rev. E*, 48:R29–R32, Jul 1993. doi: 10.1103/PhysRevE.48.R29. URL <https://link.aps.org/doi/10.1103/PhysRevE.48.R29>.
- [21] C. Meneveau. Transition between viscous and inertial-range scaling of turbulence structure functions. *Phys. Rev. E*, 54:3657–3663, Oct 1996.
- [22] C. Meneveau and K. R. Sreenivasan. Measurement of $f(\alpha)$ from scaling of histograms, and applications to dynamical systems and fully developed turbulence. *Physics Letters A*, 137(3):103 – 112, 1989.
- [23] R. J. Adler. *The geometry of random fields*. SIAM, 2010.
- [24] D. Novikov, H. A. Feldman, and S. F. Shandarin. Minkowski functionals and cluster analysis for cmb maps. *International Journal of Modern Physics D*, 8(03):291–306, 1999.
- [25] K. R. Mecke, T. Buchert, and H. Wagner. Robust morphological measures for large scale structure in the universe. *Astron. Astrophys.*, 288:697–704, 1994.
- [26] M. A. A. Calvo, S. F. Shandarin, and A. Szalay. Geometry of the cosmic web: Minkowski functionals from the delaunay tessellation. In *Voronoi Diagrams in Science and Engineering (ISVD), 2010 International Symposium on*, pages 235–243. IEEE, 2010.
- [27] A. Vincent and M. Meneguzzi. The spatial structure and statistical properties of homogeneous turbulence. *Journal of Fluid Mechanics*, 225:1–20, 1991.
- [28] J. Jimnez, A. A. Wray, P. G. Saffman, and R. S. Rogallo. The structure of intense vorticity in isotropic turbulence. *Journal of Fluid Mechanics*, 255:6590, 1993. doi: 10.1017/S0022112093002393.
- [29] C. Meneveau, K. R. Sreenivasan, P. Kailasnath, and M. S. Fan. Joint multifractal measures: Theory and applications to turbulence. *Phys. Rev. A*, 41:894–913, Jan 1990.
- [30] C. Meneveau. Lagrangian dynamics and models of the velocity gradient tensor in turbulent flows. *Annual Review of Fluid Mechanics*, 43:219–245, 2011.
- [31] Y. Li, E. Perlman, M. Wan, Y. Yang, C. Meneveau, R. Burns, S. Chen, A. Szalay, and G. Eyink. A public turbulence database cluster and applications to study lagrangian evolution of velocity increments in turbulence. *Journal of Turbulence*, (9):N31, 2008.
- [32] A. Bershadskii, E. Kit, A. Tsinober, and H. Vaisburd. Strongly localized events of energy, dissipation, enstrophy and enstrophy generation in turbulent flows. *Fluid Dynamics Research*, 14(2):71 – 101, 1994. ISSN 0169-5983.
- [33] Y. Zhu and R. A. Antonia. On the correlation between enstrophy and energy dissipation rate in a turbulent

- wake. *Applied Scientific Research*, 57(3):337–347, Sep 1996.
- [34] D. A. Donzis, P. K. Yeung, and K. R. Sreenivasan. Dissipation and enstrophy in isotropic turbulence: Resolution effects and scaling in direct numerical simulations. *Physics of Fluids*, 20(4):045108, 2008. doi: 10.1063/1.2907227.
- [35] An experimental investigation on lagrangian correlations of small-scale turbulence at low reynolds number. *Journal of Fluid Mechanics*, 574:405427, 2007. doi: 10.1017/S0022112006004204.
- [36] B. B. Mandelbrot. *The Fractal Geometry of Nature*. Henry Holt and Company, 1982. ISBN 9780716711865. URL <https://books.google.com/books?id=OR2LkE3N7-oC>.
- [37] P. L. Johnson and C. Meneveau. A closure for lagrangian velocity gradient evolution in turbulence using recent-deformation mapping of initially gaussian fields. *Journal of Fluid Mechanics*, 804:387419, 2016. doi: 10.1017/jfm.2016.551.
- [38] M. J. Turk, B. D. Smith, J. S. Oishi, S. Skory, S. W. Skillman, T. Abel, and M. L. Norman. yt: A Multi-code Analysis Toolkit for Astrophysical Simulation Data. *The Astrophysical Journal Supplement Series*, 192:9, January 2011.
- [39] H. G. E. Hentschel and I. Procaccia. The infinite number of generalized dimensions of fractals and strange attractors. *Physica D: Nonlinear Phenomena*, 8(3):435–444, 1983.
- [40] P. L. Johnson and C. Meneveau. Large-deviation joint statistics of the finite-time lyapunov spectrum in isotropic turbulence. *Physics of Fluids*, 27(8):085110, 2015.
- [41] V. Borue and S. A. Orszag. Local energy flux and subgrid-scale statistics in three-dimensional turbulence. *Journal of Fluid Mechanics*, 366:131, 1998.
- [42] P. Vieillefosse. Local interaction between vorticity and shear in a perfect incompressible fluid. *Journal de Physique*, 43(6):837–842, 1982.
- [43] C. Meneveau. Lagrangian dynamics and models of the velocity gradient tensor in turbulent flows. *Annual Review of Fluid Mechanics*, 43:219–245, 2011.
- [44] A. Naso, A. Pumir, and M. Chertkov. Statistical geometry in homogeneous and isotropic turbulence. *Journal of Turbulence*, 8:N39, 2007. doi: 10.1080/14685240701615978.
- [45] J. Martín, A. Ooi, M. S. Chong, and J. Soria. Dynamics of the velocity gradient tensor invariants in isotropic turbulence. *Physics of Fluids*, 10(9):2336–2346, 1998.
- [46] J. C. R. Hunt, A. A. Wray, and P. Moin. Eddies, streams, and convergence zones in turbulent flows. 1988.
- [47] M. S. Chong, A. E. Perry, and B. J. Cantwell. A general classification of three-dimensional flow fields. *Physics of Fluids*, 2:765–777, May 1990.

Appendix A: Analysis environment on SciServer, and notebooks

The data used in this paper is obtained from the Johns Hopkins Turbulence Databases (JHTDB). Most prior uses of JHTDB focussed on analysis of spatially localized regions, for which local operations such as interpolation or finite-difference based differentiations could be done on the database system itself and delivering small amounts of data to users. In the present work we desired instead to use FFTs for the analysis in order to enable us spectral accuracy for derivative evaluations, as well as efficient evaluation of the 3D correlation functions. However, FFTs require access to the entire 1024^3 fields, for which the usual access modes of JHTDB are not well suited. Instead, the analysis presented in this paper was performed on the Sciserver cloud environment, hosted by the Institute for Data Intensive Science at Johns Hopkins University (<http://www.sciserver.org>). The goal of Sciserver is to provide a local environment for data driven science. Sciserver provides a 10 Gigabit Ethernet connection to the Johns Hopkins Turbulence Database [31, 37], which is a valuable asset to the present work since it allows to easily download entire snapshots from the database. Sciserver was initially developed to be used in conjunction with the Sloan Digital Sky Survey, in the form of Skyserver, as a nearline analysis tool to the Astronomy database. It has since then expanded to other areas of scientific research including Turbulence, Genomics and Oceanography.

We utilized the Compute module of Sciserver, which provides a Jupyter notebook environment running over Docker containers that provide user package customizability through Anaconda and Pip package managers. Sciserver also provides a set of pre-configured docker containers for Python, Matlab and other languages.

(a) Volume rendering script with YT library:

```
In [13]: %matplotlib inline
#####
### Create the base scene from the dataset ###
#####
sc = yt.create_scene(ds, 'entrophy', lens_type='perspective')
#####
#####
zom = 0.8
sc.camera.resolution = (2024, 2024)
sc.camera.set_position(np.array([-1.5*zom*(2*np.pi)/(4), 0.0, 1.5*zom*(2*np.pi)/(4)]))
sc.camera.set_focus(ds.domain_center)
#sc.camera.roll((0.5*np.pi/2))
sc.camera.zoom(2.4)
#####
### Transfer Function / Color Options ###
#####
source = sc[0]
tf = yt.ColorTransferFunction(np.log10((w2min,w2max)))
tf.add_layers(12, colormap='inferno')
source.tff = tf
source.tff.bounds = (w2min,w2max)
source.tff.set_log(True)
source.tff.grey_opacity = False
source.tff.plot('transfer_function.png', profile_field='entrophy')
#####
### Showing and rendering the scene ###
#####
sc.show(sigma_clip=4.0)
sc.save('entrophy-volume-excursion-20.png', sigma_clip=2.0)
yt: [INFO] | 2017-06-11 17:29:52,218 Rendering scene (Can take a whi
```

(b) Two-point correlation function:

```
In [17]: start = time.time()
chi = np.zeros((N,N), dtype='float32')
cchi = ft.zeros_aligned((N,N,1+(N/2)), dtype='complex64')
corr = np.zeros((N,N), dtype='float32')
end = time.time()
print("time : "+str(end-start))
time : 21.3893649578

In [18]: iCorr = np.zeros((N//2,N//2,N//2), dtype='float32')

In [19]: start = time.time()
t=20
chi[:, :, :] = 0
chi[w2 > t*avg0] = 1
fo[:, :, :] = chi[:, :, :]
fft_object.update_arrays(fo, bo)
fft_object.execute()
cchi[:, :, :] = bo[:, :, :]
tmp = cchi*(cchi.conj())
bo[:, :, :] = tmp[:, :, :]
ifft_object.update_arrays(bo, fo)
ifft_object.execute()
corr[:, :, :] = fo[:, :, :]/(N**3)
iCorr[0:(N//2), 0:(N//2), 0:(N//2)] = corr[0:(N//2), 0:(N//2), 0:(N//2)]
corrLoc, r2edges = np.histogram(r2rt, range=(minrt, maxrt), bins = rbins, weigh
r2Loc, r2edges = np.histogram(r2rt, range=(minrt, maxrt), bins = rbins)
end = time.time()
print("time : "+str(end-start))
time : 292.268857002
```

FIG. 17: Code snippets used in the Sciserver environment : (a) Volume rendering script with YT library; (b) Two-point correlation function

The notebook runs on a docker container with access to 24 CPU cores and 256 Gigabytes of RAM. The docker container runs on top of a virtual machine (VM), which is shared among many containers.

Most of the analysis was done running Python code on the Jupyter notebooks, which allow us to integrate data analysis and documentation. Some of the most compute intensive figures were produced on Python running on batch mode instead of inside the notebook, more specifically figures Fig. (10) and Fig. (16)c, which corresponds to the fractal dimension for the iso-sets for, respectively, joint entrophy and strainrate, and joint Q and R . These calculations required the evaluation of forward and inverse 3D FFTs for each of the 120×120 geometric sets, i.e. a significant computational effort. To perform the 3D FFTs efficiently, a data-cube must fit in the RAM of a single compute node.

The present analysis mode shows that, under appropriate circumstances, using Python on Jupyter notebooks within Sciserver is a viable option to perform global analysis of large DNS datasets that have been stored in a database such as JHTDB.

Appendix B: Tests of correlation and box-counting on known fractal sets in 3D: Menger Sponge

In order to validate our techniques and present a known reference for the scaling tools utilized in this work, we present here the results of the correlation-function and box-counting based analysis for a known self-similar fractal (the Menger Sponge).

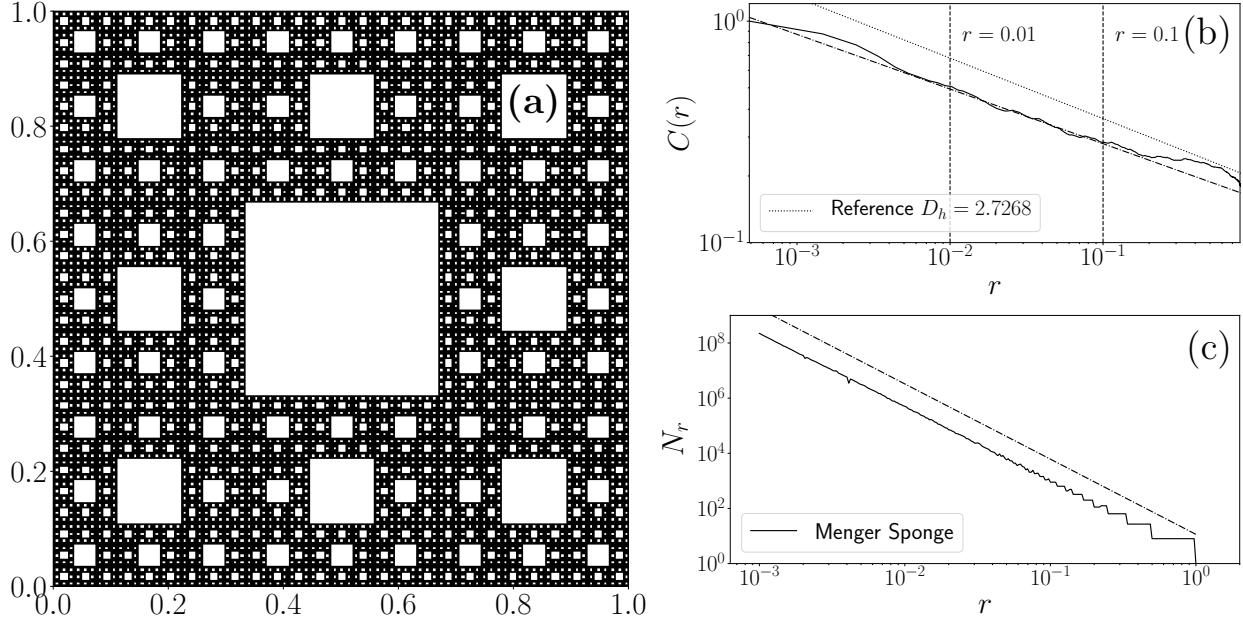


FIG. 18: (a): Contour plot of a planar cut through an indicator function marking a 5-level Menger Sponge set; (b) Two-point radial correlation function for the Menger Sponge set; (c) Box counting plot. The dotted line is the slope corresponding to the analytically known fractal dimension of the Menger Sponge ($D_0 = D_2 = \log(20)/\log(3)$).

The Menger Sponge is generated through an iterative process, in which the central $1/3$ sized sub-cube on each of the 6 sides and the core of the mother cube are deleted. This process is repeated iteratively for each remaining sub-cube. In our tests, we use a level 5 Menger sponge, i.e. the 5th iteration of removal as shown in figure 18(a). The set indicator function is computed over the same $N^3 = 1024^3$ used for the dataset of this work, in which the removed regions are set to 0, and the rest is set to 1 (on elements of scale $1024/3^5 \sim 4$).

Over this indicator function, we compute the two-point correlation function just as in section II, which results in figure 18(b). The power-law behavior is affected at large and small scales due to the cubic symmetry of the set being analyzed via spherical bins of distances. Still, there is clearly a power-law in a central decade in figure 18(b) with a slope consistent with a correlation-function based dimension of $3 - \gamma = \log 20 / \log 3$, the Hausdorff dimension of the Menger sponge. Analogously, we computed the box-counting graph for the same indicator function. Since the box-counting method is consistent with the artificial fractal set's construction, one obtains a clearer power law, as seen in figure 18(c). Again, the slope is consistent with the Hausdorff dimension. These tests verify our method of computing correlation function and box-counting based scaling exponents.